nature communications

Article

https://doi.org/10.1038/s41467-025-61078-5

Ruddlesden-Popper chalcogenides push the limit of mechanical stiffness and glass-like thermal conductivity in single crystals

Received: 22 October 2024

Accepted: 12 June 2025

Md Shafkat Bin Hoque[1,17], Eric R. Hoglund[2,3,17], Boyang Zhao[4,17], De-Liang Bao[5], Hao Zhou[6], Sandip Thakur[7], Eric Osei-Agyemang[8], Khalid Hattar[9,10], Ethan A. Scott[1,10], Mythili Surendran[4], John A. Tomko[1], John T. Gaskins[11], Kiumars Aryana[1], Sara Makarem[2], Adie Alwen[4], Andrea M. Hodge[4], Ganesh Balasubramanian[12], Ashutosh Giri[7], Tianli Feng[6], Jordan A. Hachtel[3], Jayakanth Ravichandran[4,13,14], Sokrates T. Pantelides[5,15] & Patrick E. Hopkins[1,2,16]

Insulating materials featuring ultralow thermal conductivity for diverse applications also require robust mechanical properties. Conventional thinking, however, which correlates strong bonding with high atomic-vibration-mediated heat conduction, led to diverse weakly bonded materials that feature ultralow thermal conductivity and low elastic moduli. One must, therefore, search for strongly-bonded single crystals in which heat transport is impeded by other means. Here, we report intrinsic, glass-like, ultralow thermal conductivity and ultrahigh elastic-modulus/thermal-conductivity ratio in single-crystalline Ruddlesden-Popper $Ba_{n+1}Zr_nS_{3n+1}$, $n = 2, 3$, which are derivatives of $BaZrS_3$. Their key features are strong anharmonicity and intra-unit-cell rock-salt blocks. The latter produce strongly bonded intrinsic superlattices, impeding heat conduction by broadband reduction of phonon velocities and mean free paths and concomitant strong phonon localization. The present study initiates a paradigm of “mechanically stiff phonon glasses”.

Designing materials with ultralow thermal conductivity (κ) without reducing their density and degrading their mechanical properties typically evades century-old theories on microscopic heat conduction. In non-metallic crystals, the primary modes of thermal transport are lattice vibrations, namely phonons. Dating back to theories originally pioneered by Peierls, Leibfreid and Schlomann, Einstein, and Debye, the thermal transport of atomic vibrations is directly related to the interatomic bond strengths[1–9]. Hence, “ultralow" thermal conductivity

---

[1]Department of Mechanical and Aerospace Engineering, University of Virginia, Charlottesville, VA, USA. [2]Department of Materials Science and Engineering, University of Virginia, Charlottesville, VA, USA. [3]Center for Nanophase Materials Sciences, Oak Ridge National Laboratory, Oak Ridge, TN, USA. [4]Mork Family Department of Chemical Engineering and Materials Science, University of Southern California, Los Angeles, CA, USA. [5]Department of Physics and Astronomy, Vanderbilt University, Nashville, TN, USA. [6]Department of Mechanical Engineering, University of Utah, Salt Lake City, UT, USA. [7]Department of Mechanical, Industrial, and Systems Engineering, University of Rhode Island, Kingston, RI, USA. [8]Department of Materials Design and Innovation, University at Buffalo, The State University of New York, Buffalo, NY, USA. [9]Nuclear Engineering, University of Tennessee, Knoxville, TN, USA. [10]Sandia National Laboratories, Albuquerque, NM, USA. [11]Laser thermal analysis, Charlottesville, VA, USA. [12]Department of Mechanical and Industrial Engineering, University of New Haven, West Haven, CT, USA. [13]Core Center for Excellence in Nano Imaging, University of Southern California, Los Angeles, CA, USA. [14]Ming Hsieh Department of Electrical and Computer Engineering, University of Southern California, Los Angeles, CA, USA. [15]Department of Electrical and Computer Engineering, Vanderbilt University, Nashville, TN, USA. [16]Department of Physics, University of Virginia, Charlottesville, VA, USA. [17]These authors contributed equally: Md Shafkat Bin Hoque, Eric R. Hoglund, Boyang Zhao. e-mail: j.ravichandran@usc.edu; pantelides@vanderbilt.edu; phopkins@virginia.edu

in solids often comes at the cost of "weak" interatomic-bond strength and "soft" elastic modulus (*E*), limiting their mechanical performance[10–14]. In recent years, a family of halide perovskite-structure crystalline solids has been found to feature ultralow thermal conductivities, of order 0.15–0.3 W m^{-1} K^{-1}, but their weak van der Waals (vdW) bonding leads to very low values of elastic and shear moduli[15–20]. Breaking this Pareto-normality in the design of crystals to create ultrahigh E/κ materials must, therefore, involve different strategies than those traditionally proposed to limit phonon transport. Such decoupling would have major implications for both inorganic and organic materials in many technological applications[21]. As materials such as thermal barrier coatings and thermoelectrics are subjected to large thermal gradients and intensive cycling, low thermal conductivity and high elastic modulus are often desired for better efficiency and crack propagation resistance[22–28]. Thermally insulating and mechanically strong materials are also coveted in metal contact adjacents to prevent failure from electromigration[29–31].

To overcome the barriers of achieving ultrahigh E/κ materials and create new directions for achieving single crystals with ultralow thermal conductivity, one seeks to inhibit the propagation of phonons in a "hard" lattice. In perfect crystals, phonons travel with intrinsic group velocities and are inhibited by phonon-phonon scattering caused by anharmonic effects. Historically, chalcogenides (S, Se, and Te) have been investigated for ultralow thermal conductivity because of strong anharmonicity (e.g., PbSe, Bi_2Te_3, SnSe)[32–36]. However, many of these materials tend to crystallize in layered structures with vdW interactions, leading to poor mechanical properties across the layers due to ease of shearing. Thus, covalently-bonded layered chalcogenides present a potential pathway to low thermal conductivity and high elastic modulus in the direction across the layers. We, therefore, present Ruddlesden-Popper (RP) sulfides[37,38] as potential candidates for this scenario. Unlike some RP halide perovskites that are bonded by weak vdW forces,[16,19] the RP sulfides hold both the promise of high anharmonicity and strong bonding in a layered, superlattice-like structure with intrinsic interfaces.

Herein, we report on the ultralow thermal conductivity of RP phases $Ba_{n+1}Zr_nS_{3n+1}$, $n = 2$ and 3 of barium zirconium sulfide ($BaZrS_3$)[38,39] single crystals, enabled by strong anharmonicity and a large fraction of localized and low-velocity vibrational modes throughout the entire vibrational spectrum, thus achieving broadband attenuation of thermal transport. We reveal the origin of the ultralow thermal conductivities in these RP derivatives of the chalcogenide perovskite $BaZrS_3$ using a combination of experiments and first-principles- and machine learning-driven computational approaches. Unlike previously studied vdW layered crystals, including the RP halides,[16,19] the strong Ba-S and Zr-S chalcogenide bonds across the rock-salt layers and the $(BaZrS_3)_n$ layers bring elastic-moduli values of the RP phases nearly an order of magnitude higher than other ultralow-thermal-conductivity inorganic crystals. As a result, the RP phases of these single crystals exhibit record-setting values of E/κ for any single-crystalline material discovered to date, while maintaining glass-like, ultralow thermal conductivities. Such a useful combination of thermal and mechanical properties makes the materials highly desirable in the fields of thermal barrier coatings and thermoelectric materials[40].

Results and discussion

To investigate the impact of sub-unit cell structures on thermal conductivity, we consider perovskite $BaZrS_3$ and two RP phases, $Ba_3Zr_2S_7$ and $Ba_4Zr_3S_{10}$, whose crystal structures are investigated by X-ray diffraction in Supporting Information section S1. The perovskite shown in Fig. 1a consists of tilted ZrS_6 octahedra (Fig. 1c) and BaS_{12} polyhedra (Fig. 1d). The RP-phase $Ba_3Zr_2S_7$ shown in Fig. 1b contains two perovskite sections (red brackets) that are separated by rock-salt packed layers (Fig. 1e). $Ba_4Zr_3S_{10}$ differs from $Ba_3Zr_2S_7$ by adding one more BaS and ZrS_2 atomic layer to each perovskite section. Fig. 1f shows an iDPC image of $BaZrS_3$ and Fig. 1g, h show the layered periodic stacking of perovskite layers in the two RP phases with the enlarged regions of interest, emphasizing one of two rock-salt layers that are present in a single unit cell. The elemental maps generated by electron-energy-loss spectroscopy (EELS) and the corresponding atomic-number-contrast (Z-contrast) image shown in Fig. 1(i-l) show the high degree of chemical ordering in each sublattice and the change in local symmetry at the rock-salt layers.

To understand the bonding in the RP phases, density functional theory (DFT) calculations were performed on $Ba_3Zr_2S_7$ to calculate the valence electron density, as shown in Fig. 1m, n. A line profile along the dashed white line in Fig. 1m is shown in Fig. 1o for a more quantitative evaluation. The valence electron density within the rock-salt regions is non-zero and comparable to those inside the perovskite blocks, which suggests similar intra- and inter-perovskite-block bonding strength. In other words, the bonding in the rock-salt regions, namely across the gaps highlighted in Fig. 1(b), is not of the weak, vdW type. The overall strong bonding is also reflected in the calculated elastic moduli, which have comparable values along the cross-plane and in-plane directions. The elastic-moduli values are three to four times higher than those observed in other ultralow-thermal-conductivity halide perovskites, such as, $Cs_3Bi_2I_6Cl_3$,[17] $Cs_3Bi_2I_9$,[18] the RP-phase $Cs_2PbI_2Cl_2$[16] and several metal halide perovskites (see Supplemental Table S3). The presence of strong intra- and inter-perovskite-block bonding strength in the sulfide RP phases described here mitigate the role of bond strength in the observed ultralow thermal conductivity.

To understand phonon transport through the structures, we measured the cross-plane (*c*-axis) thermal conductivity using time-domain thermoreflectance (TDTR) from 100 to 400 K, as shown in Fig. 2a. The thermal conductivities exhibit several unusual features for single-crystalline materials. First, the thermal conductivity of crystalline $BaZrS_3$ increases from 100 to 250 K, then remains relatively temperature independent. Such trend is observed in amorphous materials and disordered crystals, but it is rare in single crystals[7]. The weak or negligible temperature dependence cannot be explained by prior first-principles three-phonon scattering calculations[41] (the purple dashed curve in Fig. 2a). In contrast, our DFT-based machine-learning-interatomic-potential (MLIP)-driven molecular-dynamics (MD) simulation results (orange open dots in Fig. 2a) show good overall agreement with experimentally measured data, with only small differences above 200 K. This agreement demonstrates the accuracy of MLIP-MD (or MLMD) simulations, which implicitly capture all the atomic-vibration contributions to thermal conductivity, including the effects of three-phonon scattering, four-phonon scattering, finite-temperature phonon renormalization, temperature correction to force constant, and diffuson contributions[42,43]. This agreement also confirms that the glass-like thermal conductivity trend of single-crystalline $BaZrS_3$ is not from extrinsic defects, but rather mechanisms intrinsic to the crystal. However, the exact mechanism behind the temperature trend in the thermal conductivity of single-crystalline $BaZrS_3$ remains an open question. Supporting Figure S11 shows that perovskites have been reported to exhibit both glass- and crystalline-like thermal conductivity trends. Isolating the mechanisms that underlie the thermal conductivities observed in this class of materials is beyond the scope of the present study, as we focus on the RP phases.

The RP phases $Ba_3Zr_2S_7$ and $Ba_4Zr_3S_{10}$ possess ultralow thermal conductivities, i.e., 0.45 ± 0.07 and 0.42 ± 0.05 W m^{-1} K^{-1}, respectively, over a relatively large temperature range. These values are ~3.5 times lower than those of single-crystalline $BaZrS_3$, in agreement with the Agne et al.'s diffuson limit,[6] and lower than Cahill et al.'s glass limit[4]. These two limits are two of the most commonly used theoretical models to predict the lowest possible thermal conductivity of a crystalline material. Additionally, the thermal conductivities of $Ba_3Zr_2S_7$ (green diamonds) and $Ba_4Zr_3S_{10}$ (blue triangles) show glass-like temperature trends, comparable to that of amorphous $BaZrS_3$ (black circles). The MLMD thermal conductivity simulations of $Ba_3Zr_2S_7$ show quantitative agreement with the experimental data. The cross-plane thermal conductivities of the sulfide RP phases are even lower than those of vdW layered materials, except when thin film samples and interlayer rotations are involved[10,44]. On the other hand, the sulfide RP phases feature far superior mechanical properties of all vdW layered materials.

Defects in materials have also been known to lead to ultralow thermal conductivity and glass-like temperature trends[7]. X-ray diffraction data mentioned earlier (shown in Supporting Information section S1), combined with the agreement of the simulations of the thermal conductivity with the experimental data, prove the high quality of the single crystals used in this study, which precludes the attribution of the low thermal conductivity to disorder and defects. To study how the introduction of defects would change thermal conductivity, we irradiate the $BaZrS_3$ and $Ba_4Zr_3S_{10}$ crystals with high energy gold ions. The measured cross-plane thermal conductivities of the heavily ion-irradiated crystals as a function of ion dose are shown in Fig. 2b. The thermal conductivity of $BaZrS_3$ exhibits a sigmoidal reduction, typically characteristic of irradiated crystalline materials[45,46]. At low doses, irradiation introduces low concentrations of clustered point defects and vacancies. The overall crystal structure remains relatively unchanged, whereby the thermal conductivity is nearly constant. At high doses, point-defect concentrations increase and damaged regions overlap, which gradually decreases the thermal conductivity to that of an amorphous solid.

Compared to $BaZrS_3$, a completely different thermal conductivity trend is observed vs. ion dose in the RP phases; the thermal conductivity of the $Ba_4Zr_3S_{10}$ crystals remains nearly constant regardless of gold ion dose. TEM micrographs show that the layering of $Ba_4Zr_3S_{10}$ crystals remains uninterrupted throughout the range of doses, although high doses can introduce amorphous pockets (see Supporting Information). In vdW layered materials with interlayer rotation, ion irradiation can lead to increased thermal conductivity due to increases in interatomic bonding[10]. However, due to the already strong bonding of the RP phases, no such trend is observed in the present study. The resistance of the RP crystals to irradiation damage makes them a highly suitable thermal barrier coating in deep space applications in radiation environments.

To gain insight into the role of anisotropy in ultralow thermal conductivity of the RP phases, we measure the thermal conductivity of $Ba_3Zr_2S_7$ along the in-plane direction (perpendicular to *c*-axis) at room

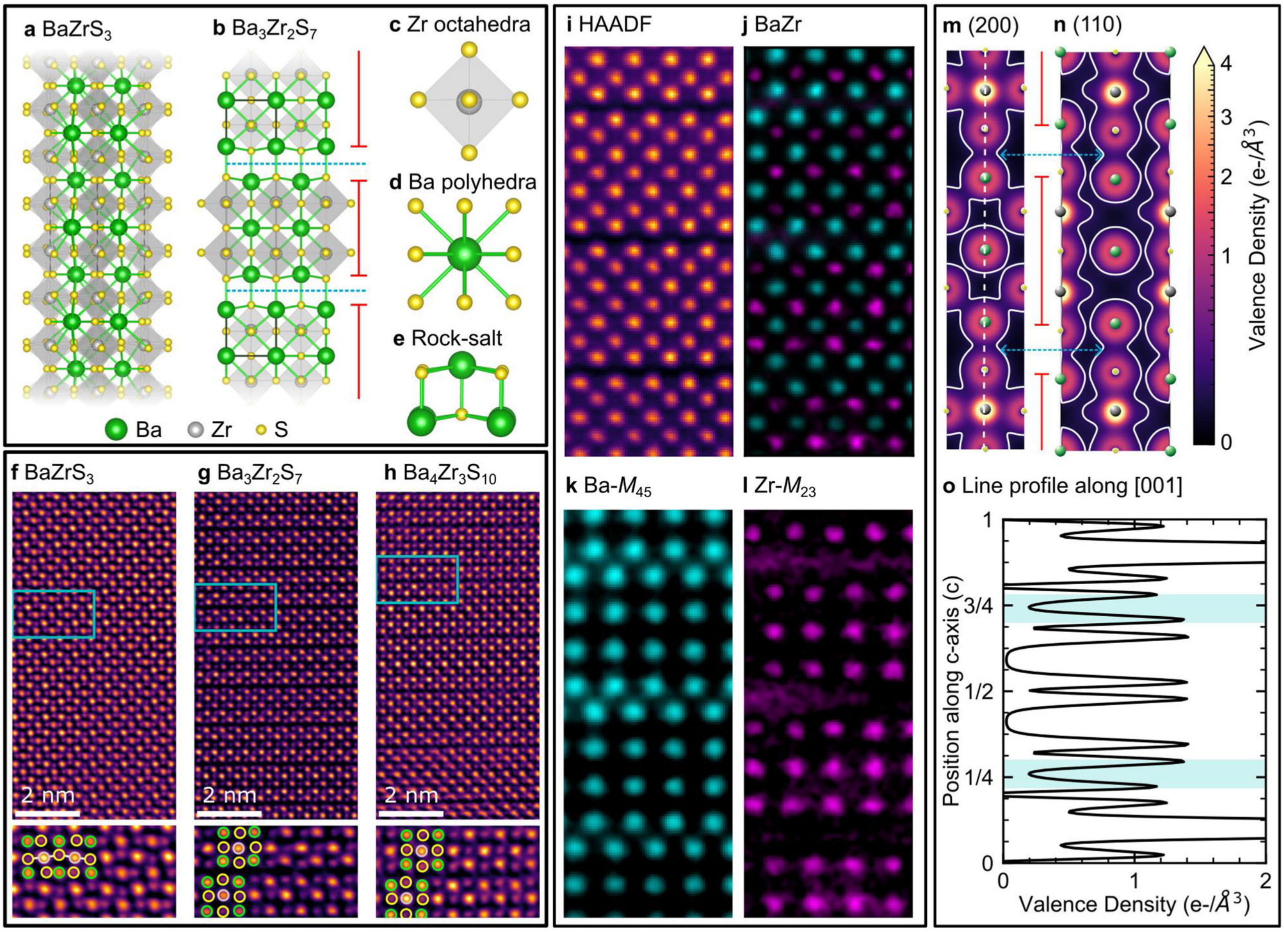

Fig. 1 | Structure of perovskite $BaZrS_3$ and Ruddlesden-Popper $Ba_{n+1}Zr_nS_{3n+1}$. Ball-and-stick model of (**a**) *Pnma* perovskite $BaZrS_3$ and (**b**) *I4mmm* Ruddlesden-Popper $Ba_3Zr_2S_7$ showing gray ZrS_6 octahedra and green BaS bonds. Red markers in (**b**) indicate the perovskite blocks of the RP phase separated by the rock-salt blocks. Blue dotted lines between BaS atomic planes indicate the midplane of the rock-salt blocks. Ball-and-stick model of a (**c**) Zr octahedra, (**d**) undistorted Ba polyhedral, and (**e**) rock-salt building block resulting from layering in $Ba_3Zr_2S_7$. Integrated differential phase contrast images of the (**f**) $BaZrS_3$, (**g**) $Ba_3Zr_2S_7$, (**h**) $Ba_4Zr_3S_{10}$ crystals. Enlarged regions from the cyan annotations are shown below each image. In the enlargements, two perovskite unit cells are annotated with Ba (green), Zr (gray) and S (yellow) circles. (**i**) Z-contrast image and (**j**) BaZr composite image from a STEM-EELS spectrum image. Intensity maps of (**k**) Ba-M_{45}, (**l**) Zr-M_{23} background-subtracted edges. **m**, **n** Section views along (200) and (110) of the valence electron density of the RP-phase $Ba_3Zr_2S_7$ calculated by DFT, respectively. Red marks and blue dashed lines help to correlate atomic structure to that of panel (**b**). **o** A line profile of the valence electron density along the white dashed line in (**m**). Blue bars illustrate the rock-salt-block regions.

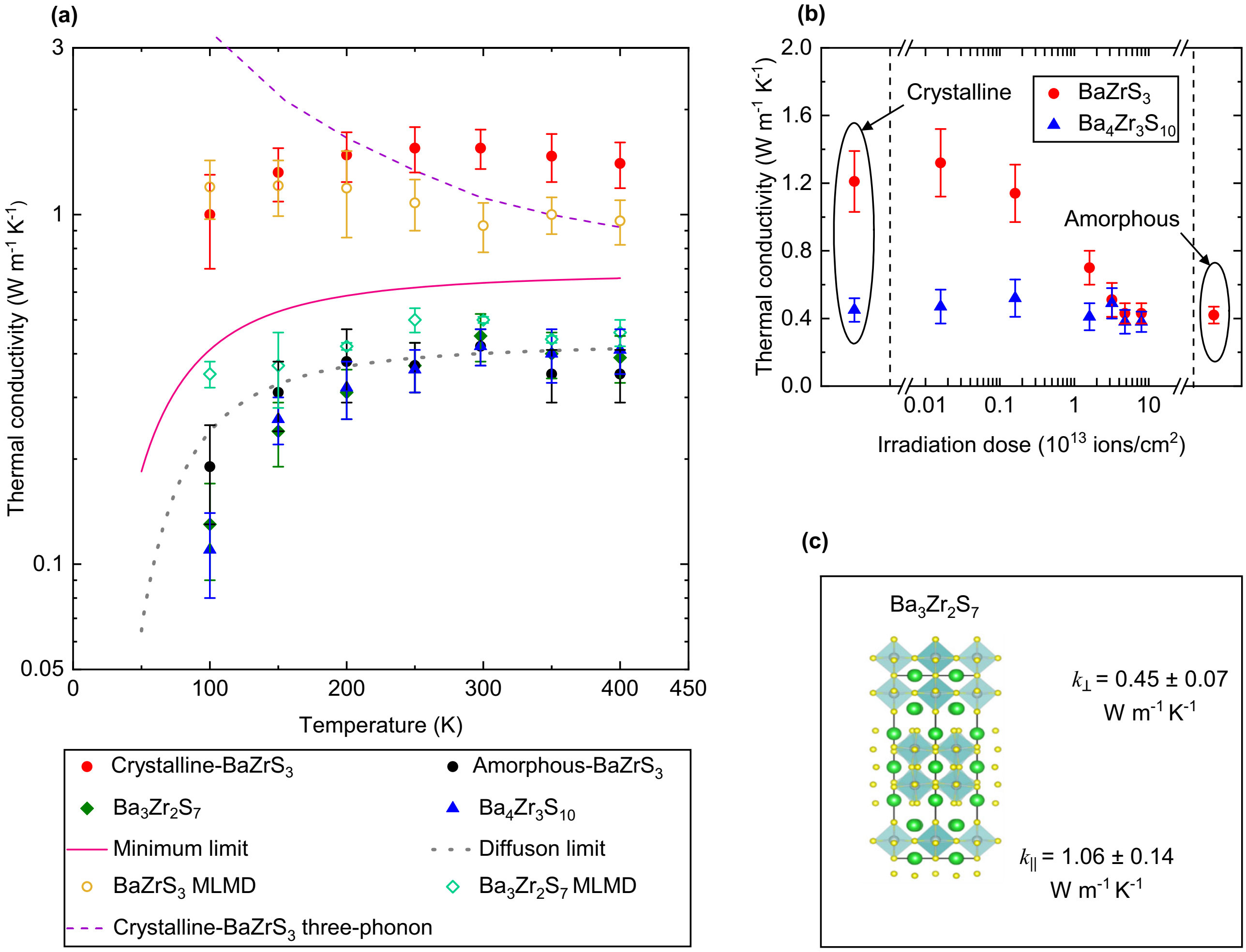

Fig. 2 | Thermal conductivities - experimental and simulated. a TDTR-measured cross-plane thermal conductivity of $BaZrS_3$ and its RP derivatives. For comparison, we also include the three-phonon and MLMD predicted thermal conductivity of $BaZrS_3$ and RP phases. The three-phonon prediction is adopted from Osei-Agyemang et al.[41] The minimum limit and diffuson limit refer to Cahill et al.[4] and Agne et al.'s[6] theoretical models. **b** Thermal conductivity distribution of $BaZrS_3$ and RP phases as a function of heavy ion-irradiation doses. The thermal conductivity of the crystalline $BaZrS_3$ is lower compared to panel (**a**) due to the presence of nano-domains (see Supporting Information for details). **c** Anisotropic thermal conductivity of $Ba_3Zr_2S_7$ measured by TDTR at room temperature. The uncertainty/error bars of the measurements are discussed in the Supporting Information.

temperature as shown in Fig. 2c. The in-plane thermal conductivity is 1.06 ± 0.14 W m^{-1} K^{-1} which is ~2.5 times higher than the cross-plane thermal conductivity (0.45 ± 0.07 W m^{-1} K^{-1}). It is noteworthy that the MLMD-simulated in-plane and cross-plane thermal conductivities are 1.02 ± 0.17 and 0.53 ± 0.02 W m^{-1} K^{-1}, respectively, showing excellent quantitative agreement with the experimental anisotropy. The agreement combined with the X-ray diffraction data rule out the impact of defects on measured thermal conductivities. The major structural difference between the in-plane and cross-plane directions is the periodic rock-salt and perovskite layers, relative to continuous layers in-plane. This result suggests that, despite the strong bonding, the rock-salt layers are causing the ultralow and anisotropic thermal conductivity in the RP phases.

To understand how the introduction of rock-salt layering leads to the ultralow thermal conductivities in the RP phases compared to that of crystalline $BaZrS_3$, we consider three factors that may contribute to ultralow thermal conductivity: 1) anharmonic scattering, 2) decreased phonon group velocities (v_g), and 3) phonon localization within unit cells[47].

To assess the role of anharmonic scattering, we calculated the spectral energy density (SED) of $BaZrS_3$ and $Ba_3Zr_2S_7$ based on MLMD, as shown in Fig. 3a, b. Compared to a typical semiconductor (e.g., silicon, gallium nitride), the SEDs of both $BaZrS_3$ and $Ba_3Zr_2S_7$ show much more blurred and broadened linewidths, indicating strong anharmonicity and large phonon scattering rates[47,48]. These features could be a critical reason for the ultralow thermal conductivity. The large overlapping of branches due to the anharmonic broadening also indicates that the interband tunneling (i.e., diffusons) should be significant, based on the Wigner formalism[49,50]. This feature could be a reason for the glass-like thermal conductivity exhibited by the experimental data. Recent calculations using the Wigner formalism show that diffuson contributes 30% to thermal conductivity of $BaZrS_3$. We expect the diffuson contribution to be even larger in $Ba_3Zr_2S_7$ since the broadening of SED is more significant.

Group velocity (v_g) is another important parameter to understand the diffusivity of vibrational modes in a material[13]. The group velocities along the cross-plane direction ($v_{g,z}$) of $BaZrS_3$ and $Ba_3Zr_2S_7$ are compared in Fig. 3c. Despite the presence of strong intra- and inter-perovskite-block bonding strength in $Ba_3Zr_2S_7$, its cross-plane phonon modes have smaller group velocities at nearly all frequencies with relatively flat dispersions. Though weak cross-plane bonding (e.g., in van der Waals layered materials) results in relatively flat bands, the reverse is not true as strongly bonded materials often have flat bands. For example, optical phonon bands are often relatively flat in strongly

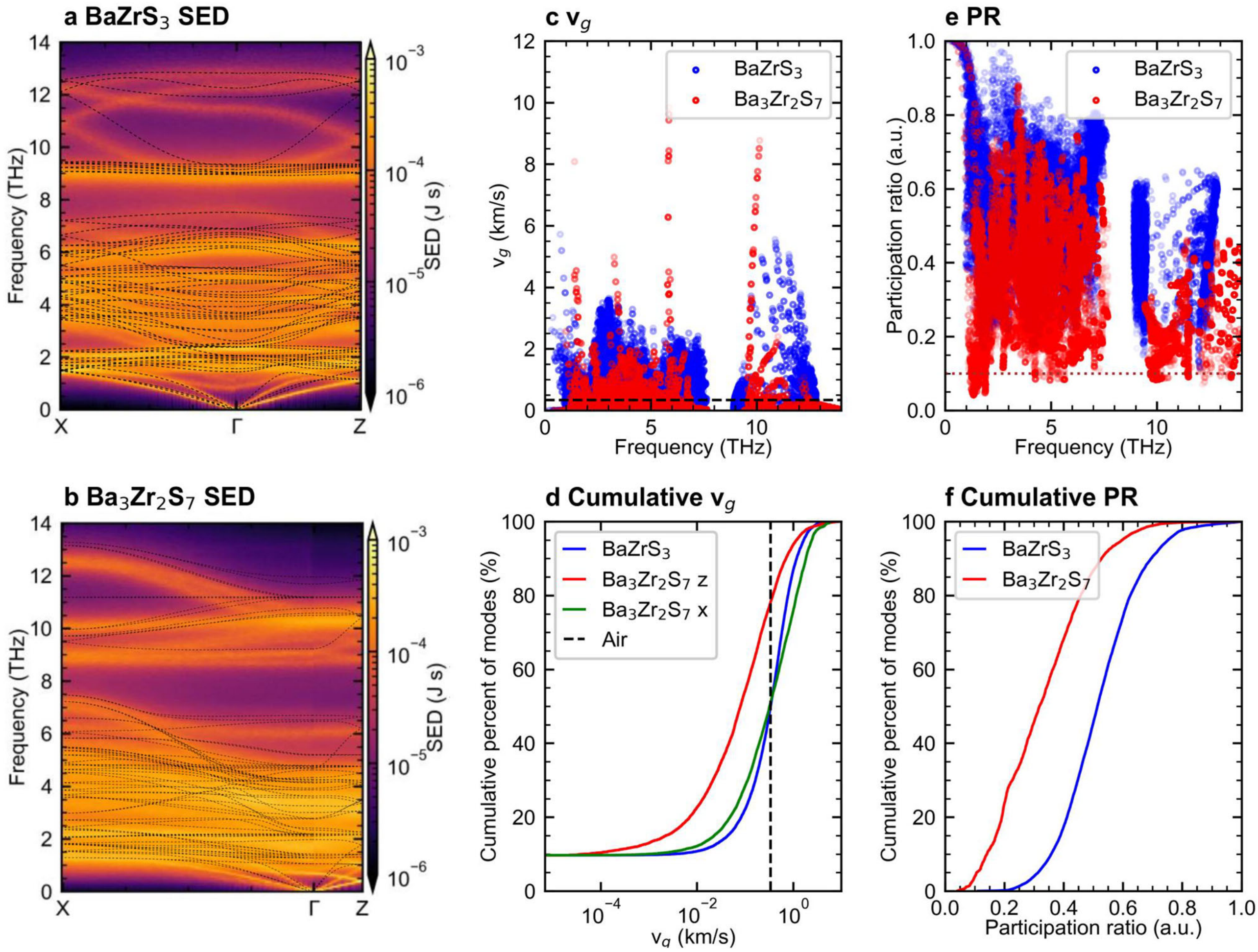

Fig. 3 | Evaluation of factors that influence thermal conductivity. Spectral energy density calculated from MLMD for (**a**) $BaZrS_3$ and (**b**) $Ba_3Zr_2S_7$. The overlays are the harmonic dispersions of phonons in $BaZrS_3$ and $Ba_3Zr_2S_7$, which contrast with the blurred SED (SEDs for materials with negligible anharmonic effects look very much like the corresponding harmonic dispersions, as we show in the case of silicon in Supplemental Figure S19). **c** v_g of the $BaZrS_3$ and RP structure along the cross-plane direction as a function of frequency with the dashed black line serving as a reference for air. **d** Cumulative number of phonon modes having up to a given group velocity as a function of frequency for the crystals along cross- (*z*) and in- (*x*) plane directions. **e** Participation ratio (PR) as a function of frequency for $BaZrS_3$ and (**b**) $Ba_3Zr_2S_7$. **f** Cumulative number of phonon modes having up to a given PR as a function of frequency.

bonded materials, e.g., GaAs. Another strongly bonded material, β-Ga_2O_3, has a relatively large number of flat bands and thus low thermal conductivity. The origin of relatively flat bands in strongly bonded materials is not always clear.

In Fig. 3d, we plot the cumulative number of phonon modes as a function of group velocity to quantify the number of modes having ultralow group velocities. We find that 80% of phonon modes of $Ba_3Zr_2S_7$ have a $v_{g,z}$ lower than the sound speed of air. In comparison, the *x* component shows a larger group velocity, which is similar to that of $BaZrS_3$. This feature would indicate that the in-plane thermal conductivity of $Ba_3Zr_2S_7$ is similar to that of $BaZrS_3$ but the cross-plane thermal conductivity would be much lower, which is consistent with both the experimental observations and the simulations. Thus, the ultralow phonon velocities, induced by the presence of periodic building blocks in unit cells, is another key contributing factor to the ultralow thermal conductivities.

The third possible factor contributing to ultralow thermal conductivity is phonon localization. We note that the ultralow group velocities of Fig. 3c, d do not inherently imply phonon localization. For example, phonons in relatively flat optical bands in GaAs have small group velocities, but are not localized anywhere because the primitive unit cell has only two atoms. To study the spatial localization of phonon waves within a unit cell of $BaZrS_3$ and $Ba_3Zr_2S_7$, we calculate the participation ratio (PR) of the vibrational modes. Localized vibrational modes are usually defined as having a participation ratio lower than 0.1[51]. As shown in Fig. 3(e,f), the participation ratio of $Ba_3Zr_2S_7$ is significantly lower than that of $BaZrS_3$ across all frequencies. It is noteworthy that some low-frequency modes (<2 THz) in the RP phase have a participation ratio that is smaller than 0.1, which is comparable to the localization expected for locons in amorphous materials[51,52]. This result provides evidence that the presence of rock-salt building block layers in the RP phases causes a significant number of vibrational modes to become highly localized[18].

To further show the localization of the vibrational modes, we estimate the average mean free path of phonons in $Ba_3Zr_2S_7$ in Supporting Figure S12. Assuming the diffuson thermal conductivity is zero, the average mean free path of phonons is estimated as 1 nm, to match with experimental thermal conductivity. Since diffuson contribution is nonzero, the actual mean free path of phonons should be smaller than 1 nm, the inter-gap thickness. These considerations indicate that the phonons are localized inside the rock-salt layers of $Ba_3Zr_2S_7$ by the gaps, being consistent with the participation ratio results.

In summary, the presence of intra-unit-cell rock-salt blocks in the sulfide RP phases derived from $BaZrS_3$ and the corresponding selenide and telluride RP phases effectively produces strongly bonded, intrinsic superlattices with different periodicities and interfacial regions that

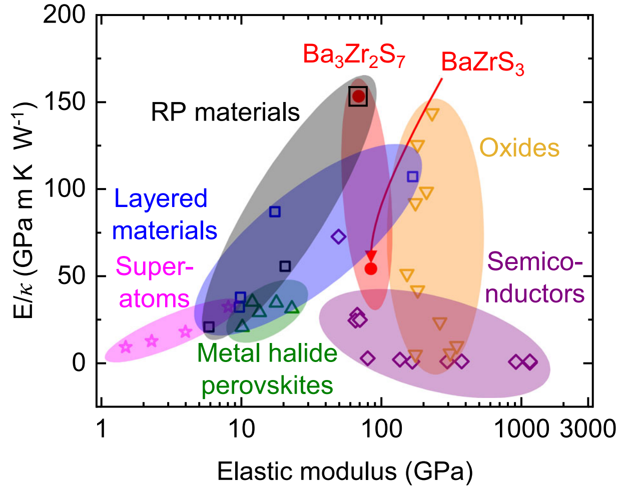

Fig. 4 | Elastic modulus/thermal conductivity (E/κ) ratio for a wide range of single-crystalline materials at room temperature. The crystals are grouped into superatoms, metal halide perovskites, semiconductors, oxides, layered materials, and $BaZrS_3$ and its RP derivatives. The thermal conductivity and elastic modulus data of the single crystals are provided in the Supporting Information.

largely reduce phonon velocities and mean free paths, inducing strong localization. Combined with the strong anharmonicity that is known to be intrinsic to chalcogenides,[32–36] the chalcogenide RP phases are a class of single-crystalline materials that can achieve broadband restriction of thermal transport, leading to ultralow thermal conductivities, while sustaining high elastic moduli and hence high E/κ ratios.

In Fig. 4, we compare the E/κ of $BaZrS_3$ and its RP derivatives with a wide range of single crystals. The materials shown here range from soft, insulating crystals (e.g., Co_6S_8) to stiff, conductive crystals (e.g., diamond). The elastic moduli of $BaZrS_3$ and RP phases are significantly higher than those of other ultralow-thermal-conductivity single crystals (e.g., superatoms, metal halide perovskites, and layered perovskites) and are surpassed only by oxides and some semiconductors. Despite such strong bonding, the RP phases possess an ultralow thermal conductivity. As a result, the E/κ ratio of the $Ba_3Zr_2S_7$ single crystal is the highest reported to date. Though some polycrystalline materials have larger E/κ ratios,[24,53] the record E/κ ratio shown in Fig. 4 among single-crystalline solids is very significant in its own right as not only it eliminates any extrinsic spurious influences in E/κ values, but also allows us to study the fundamental mechanisms behind the mechanically stiff phonon glass paradigm. Additionally, the E/κ ratio of the RP phase is ~3 times higher than that of $BaZrS_3$.

As shown in Fig. 4, oxides generally possess a high elastic modulus. By replacing oxygen with sulfur, we reduce thermal conductivity significantly with moderate reduction in the elastic modulus. Introduction of strongly bonded periodic interfaces can further reduce the thermal conductivity without sacrificing stiffness proportionately. The sulfides studied here sit in an ideal regime of relatively high elastic modulus and low thermal conductivity thereby opening a paradigm for finding high E/κ ratio materials. For example, RP phases of $BaHfS_3$ are also likely to exhibit a high E/κ ratio. Moreover, the study of chalcogenide perovskites has gained momentum only recently. We anticipate the discovery and synthesis of a broad range of layered phases such as Aurivillius phases and Dion Jacobson phases in the near future[54,55]. These layered materials will present additional opportunities to test and further the paradigm of "mechanically stiff phonon glass".

The RP phases of $BaZrS_3$ is found to possess ultralow thermal conductivity and ultrahigh modulus-to-thermal conductivity ratio. We find that the rock-salt layers separating the perovskite sections of the RP structure lead to highly anisotropic thermal conductivity, with the cross-plane reaching values comparable to the amorphous solid despite similar and highly strong bonding across the full unit cell. Together with simulations, our results provide evidence that the rock-salt layers in the single crystal RP phases lead to ultralow phonon velocities, ultrashort phonon mean free paths, and strong localization within rock-salt layers, leading to ultralow, glass-like thermal conductivity. Our study provides a detailed overview of the mechanisms needed to achieve ultralow thermal conductivity in a non-vdW, strongly bonded, layered material.

Methods

Time-domain thermoreflectance (TDTR)

We use a two-tint time-domain thermoreflectance (TDTR) setup to measure the thermal conductivity of the crystalline and amorphous $BaZrS_3$, $Ba_3Zr_2S_7$, and $Ba_4Zr_3S_{10}$ specimens[56,57]. In our TDTR setup, a Ti:sapphire oscillator (80 MHz, ~808 nm central wavelength, and ~14 nm full width at half maximum) emanates subpicosecond laser pulses that are split into a high-power pump and a low-power probe beam. The pump beam is modulated at a frequency of 8.4 MHz by an electro-optic modulator (EOM) to create oscillatory heating events at the sample surface. The probe beam is then directed through a mechanical delay stage to detect the temporal change in thermoreflectivity which is related to the surface temperature change. Using a lock-in amplifier and a balanced photodetector, the probe beam measures the temperature decay up to 5.5 ns. The TDTR data are analyzed by fitting a cylindrically symmetric, multilayer thermal model to the ratio of in-phase to out-of-phase signal ($-V_{in}/V_{out}$) from the RF lock-in amplifier[58–61].

Ion irradiation

The $BaZrS_3$ and $Ba_4Zr_3S_{10}$ single crystals are irradiated with gold (Au) ions at an energy of 2.8 MeV using a 6 MV tandem Van de Graaff accelerator. The ion implantation depths are calculated via SRIM simulations for an ion energy of 2.8 MeV. Details of the SRIM simulations for determining the stopping range of ions can be found in previous publications[46,62]. The implantation depths of the Au ions are greater than 450 nm. This length scale is much larger than the thermal penetration depth of TDTR measurements[63]. Therefore, the thermally probed region and the measured thermal conductivity are of the defected region pre-end-of-range[45,64].

Data availability

The data that support the findings of this study are available from the corresponding author upon reasonable request.

References

1. Kittel, C. Interpretation of the thermal conductivity of glasses. *Phys. Rev.* **75**, 972 (1949).
2. Ioffe, A.F., Regel, R. Non-Crystalline, Amorphous and Liquid Electronic Semiconductors. *Progress In Semiconductors*. 237–291 (Heywood and Co., Ltd., London, 1960).
3. Slack, G. A. The thermal conductivity of nonmetallic crystals. *Solid state Phys.* **34**, 1–71 (1979).
4. Cahill, D. G., Watson, S. K. & Pohl, R. O. Lower limit to the thermal conductivity of disordered crystals. *Phys. Rev. B* **46**, 6131 (1992).
5. Clarke, D. R. Materials selection guidelines for low thermal conductivity thermal barrier coatings. *Surf. Coat. Technol.* **163**, 67–74 (2003).
6. Agne, M. T., Hanus, R. & Snyder, G. J. Minimum thermal conductivity in the context of diffuson-mediated thermal transport. *Energy Environ. Sci.* **11**, 609–616 (2018).
7. Beekman, M. & Cahill, D. G. Inorganic crystals with glass-like and ultralow thermal conductivities. *Cryst. Res. Technol.* **52**, 1700114 (2017).

8. Mukhopadhyay, S. et al. Two-channel model for ultralow thermal conductivity of crystalline Tl3VSe4. *Science* **360**, 1455–1458 (2018).
9. Kim, S. E. & Cahill, D. G. Pushing low thermal conductivity to the limit. *Science* **373**, 963–964 (2021).
10. Chiritescu, C. et al. Ultralow thermal conductivity in disordered, layered WSe2 crystals. *Science* **315**, 351–353 (2007).
11. Duda, J. C., Hopkins, P. E., Shen, Y. & Gupta, M. C. Exceptionally low thermal conductivities of films of the fullerene derivative PCBM. *Phys. Rev. Lett.* **110**, 015902 (2013).
12. Wang, X., Liman, C. D., Treat, N. D., Chabinyc, M. L. & Cahill, D. G. Ultralow thermal conductivity of fullerene derivatives. *Phys. Rev. B* **88**, 075310 (2013).
13. Braun, J. L. et al. Charge-induced disorder controls the thermal conductivity of entropy-stabilized oxides. *Adv. Mater.* **30**, 1805004 (2018).
14. Qian, X., Zhou, J. & Chen, G. Phonon-engineered extreme thermal conductivity materials. *Nat. Mater.* **20**, 1188–1202 (2021).
15. Elbaz, G. A. et al. Phonon speed, not scattering, differentiates thermal transport in lead halide perovskites. *Nano Lett.* **17**, 5734–5739 (2017).
16. Acharyya, P. et al. Intrinsically ultralow thermal conductivity in Ruddlesden–Popper 2D perovskite Cs2PbI2Cl2: localized anharmonic vibrations and dynamic octahedral distortions. *J. Am. Chem. Soc.* **142**, 15595–15603 (2020).
17. Acharyya, P. et al. Glassy thermal conductivity in Cs3Bi2I6Cl3 single crystal. *Nat. Commun.* **13**, 5053 (2022).
18. Acharyya, P. et al. Extended antibonding states and phonon localization induce ultralow thermal conductivity in low dimensional metal halide. *Adv. Funct. Mater*. **33**, 2304607 (2023).
19. Christodoulides, A. D. et al. others Signatures of coherent phonon transport in ultralow thermal conductivity two-dimensional Ruddlesden–Popper phase perovskites. *ACS nano* **15**, 4165–4172 (2021).
20. Mandal, A., Goswami, S., Das, S., Swain, D. & Biswas, K. New lead-free hybrid layered double perovskite halides: synthesis, structural transition and ultralow thermal conductivity. *Angew. Chem.* **136**, e202406616 (2024).
21. Choy, C., Wong, Y., Yang, G. & Kanamoto, T. Elastic modulus and thermal conductivity of ultradrawn polyethylene. *J. Polym. Sci. Part B: Polym. Phys.* **37**, 3359–3367 (1999).
22. Snyder, G. J.Toberer, E. S. *Materials For Sustainable Energy: a collection of peer-reviewed research and review articles from Nature Publishing Group*; World Scientific, (2011).
23. Ravichandran, J. et al. others Crossover from incoherent to coherent phonon scattering in epitaxial oxide superlattices. *Nat. Mater.* **13**, 168–172 (2014).
24. Yang, J. et al. Diffused lattice vibration and ultralow thermal conductivity in the binary Ln–Nb–O oxide system. *Adv. Mater.* **31**, 1808222 (2019).
25. Aryana, K. et al. Tuning network topology and vibrational mode localization to achieve ultralow thermal conductivity in amorphous chalcogenides. *Nat. Commun.* **12**, 1–9 (2021).
26. Gibson, Q. D. et al. others Low thermal conductivity in a modular inorganic material with bonding anisotropy and mismatch. *Science* **373**, 1017–1022 (2021).
27. Thakare, J. G., Pandey, C., Mahapatra, M. & Mulik, R. S. Thermal barrier coatings-a state of the art review. *Met. Mater. Int.* **27**, 1947–1968 (2021).
28. Hu, S. Gu, X. Approaching to low thermal conductivity limit in layered materials through full-spectrum phonon band engineering. *Mater. Today Phys.* **52**, 101669 (2025).
29. Koleshko, V. & Kiryushin, I. Electromigration threshold of thin-film conductors. *Thin solid films* **192**, 181–191 (1990).
30. Tu, K.-N. Recent advances on electromigration in very-large-scale-integration of interconnects. *J. Appl. Phys.* **94**, 5451–5473 (2003).
31. Lienig, J.Thiele, M.Lienig, J.Thiele, M. *Fundamentals of Electro-migration*. (Springer, 2018).
32. Chiritescu, C.Mortensen, C.Cahill, D. G.Johnson, D. Zschack, P. Lower limit to the lattice thermal conductivity of nanostructured Bi2Te3-based materials. *J. Appl. Phys.* **106**, 073503 (2009).
33. Manley, M. E. et al. others Intrinsic anharmonic localization in thermoelectric PbSe. *Nat. Commun.* **10**, 1928 (2019).
34. Ong, W.-L. et al. Orientational order controls crystalline and amorphous thermal transport in superatomic crystals. *Nat. Mater.* **16**, 83–88 (2017).
35. Zhao, L.-D. et al. Ultralow thermal conductivity and high thermoelectric figure of merit in SnSe crystals. *Nature* **508**, 373–377 (2014).
36. Su, L. et al. High thermoelectric performance realized through manipulating layered phonon-electron decoupling. *Science* **375**, 1385–1389 (2022).
37. Niu, S. et al. others Optimal bandgap in a 2D Ruddlesden–Popper perovskite chalcogenide for single-junction solar cells. *Chem. Mater.* **30**, 4882–4886 (2018).
38. Niu, S. et al. Crystal growth and structural analysis of perovskite chalcogenide BaZrS3 and Ruddlesden–Popper phase Ba3Zr2S7. *J. Mater. Res.* **34**, 3819–3826 (2019).
39. Li, W. et al. Band gap evolution in Ruddlesden-Popper phases. *Phys. Rev. Mater.* **3**, 101601 (2019).
40. Toberer, E. S., Baranowski, L. L. & Dames, C. Advances in thermal conductivity. *Annu. Rev. Mater. Res.* **42**, 179–209 (2012).
41. Osei-Agyemang, E. & Balasubramanian, G. Understanding the extremely poor Lattice thermal transport in chalcogenide perovskite BaZrS3. *ACS Appl. Energy Mater.* **3**, 1139–1144 (2019).
42. Tiwari, J. & Feng, T. Accurate prediction of thermal conductivity of Al 2 O 3 at ultrahigh temperatures. *Phys. Rev. B* **109**, 075201 (2024).
43. Kulnitskiy, B., Blank, V., Kuznetsov, M., Nosukhin, S. & Terentiev, S. The effect of boron on the structure and lattice parameters of diamond single crystals. *Diam. Relat. Mater.* **144**, 111015 (2024).
44. Kim, S. E. et al. others Extremely anisotropic van der Waals thermal conductors. *Nature* **597**, 660–665 (2021).
45. Scott, E. A. et al. Orders of magnitude reduction in the thermal conductivity of polycrystalline diamond through carbon, nitrogen, and oxygen ion implantation. *Carbon* **157**, 97–105 (2020).
46. Scott, E. A. et al. Reductions in the thermal conductivity of irradiated silicon governed by displacement damage. *Phys. Rev. B* **104**, 134306 (2021).
47. Thomas, J. A., Turney, J. E., Iutzi, R. M., Amon, C. H. & McGaughey, A. J. Predicting phonon dispersion relations and lifetimes from the spectral energy density. *Phys. Rev. B* **81**, 081411 (2010).
48. de Koker, N. Thermal conductivity of MgO periclase from equilibrium first principles molecular dynamics. *Phys. Rev. Lett.* **103**, 125902 (2009).
49. Simoncelli, M., Marzari, N. & Mauri, F. Unified theory of thermal transport in crystals and glasses. *Nat. Phys.* **15**, 809–813 (2019).
50. Simoncelli, M., Mauri, F. & Marzari, N. Thermal conductivity of glasses: first-principles theory and applications. *npj Comput. Mater.* **9**, 106 (2023).
51. Seyf, H. R. & Henry, A. A method for distinguishing between propagons, diffusions, and locons. *J. Appl. Phys.* **120**, 025101 (2016).
52. Lv, W. & Henry, A. Non-negligible contributions to thermal conductivity from localized modes in amorphous silicon dioxide. *Sci. Rep.* **6**, 35720 (2016).
53. Guo, Y. et al. High-entropy titanate pyrochlore as newly low-thermal conductivity ceramics. *J. Eur. Ceram. Soc.* **42**, 6614–6623 (2022).
54. Kendall, K. R., Navas, C., Thomas, J. K. & zur Loye, H.-C. Recent developments in oxide ion conductors: Aurivillius phases. *Chem. Mater.* **8**, 642–649 (1996).
55. Benedek, N. A. Origin of ferroelectricity in a family of polar oxides: the Dion- Jacobson phases. *Inorg. Chem.* **53**, 3769–3777 (2014).

56. Olson, D. H. et al. Anisotropic thermal conductivity tensor of β-Y2Si2O7 for orientational control of heat flow on micrometer scales. *Acta Materialia* **189**, 299–305 (2020).
57. Olson, D. H. et al. Local thermal conductivity measurements to determine the fraction of α-cristobalite in thermally grown oxides for aerospace applications. *Scr. Materialia* **177**, 214–217 (2020).
58. Cahill, D. G., Goodson, K. & Majumdar, A. Thermometry and thermal transport in micro/nanoscale solid-state devices and structures. *J. Heat. Transf.* **124**, 223–241 (2002).
59. Cahill, D. G. Analysis of heat flow in layered structures for time-domain thermoreflectance. *Rev. Sci. Instrum.* **75**, 5119–5122 (2004).
60. Schmidt, A. J., Chen, X. & Chen, G. Pulse accumulation, radial heat conduction, and anisotropic thermal conductivity in pump-probe transient thermoreflectance. *Rev. Sci. Instrum.* **79**, 114902 (2008).
61. Hopkins, P. E. et al. Criteria for cross-plane dominated thermal transport in multilayer thin film systems during modulated laser heating. *J. Heat Transfer*, **132**, 081302 (2010).
62. Scott, E. A. et al. Thermal conductivity enhancement in ion-irradiated hydrogenated amorphous carbon films. *Nano Lett.* **21**, 3935–3940 (2021).
63. Koh, Y. K. & Cahill, D. G. Frequency dependence of the thermal conductivity of semiconductor alloys. *Phys. Rev. B* **76**, 075207 (2007).
64. Scott, E. A. et al. Probing thermal conductivity of subsurface, amorphous layers in irradiated diamond. *J. Appl. Phys.* **129**, 055307 (2021).

Acknowledgements

We thank Kevin Ye and Rafael Jaramillo from Department of Materials Science and Engineering of Massachusetts Institute of Technology for their help with the sample preparation. M.S.B.H., E.A.S., J.A.T., S.M., K.A. and P.E.H. appreciate support from the Office of Naval Research Grant No. N0014-23-1-2630. E.R.H. and J.A.H. acknowledge that vibrational EELS experiments were supported by the U.S. Department of Energy, Office of Basic Energy Sciences (DOE-BES), Division of Materials Sciences and Engineering under contract ERKCS8 and was performed at the Center for Nanophase Materials Sciences, (CNMS), which is a DOE Office of Science User Facility using instrumentation within ORNL's Materials Characterization Core provided by UT-Battelle, LLC, under Contract No. DE-AC05- 00OR22725 with the DOE and sponsored by the Laboratory Directed Research and Development Program of Oak Ridge National Laboratory, managed by UT-Battelle, LLC, for the U.S. Department of Energy. D.-L.B. and S.T.P. acknowledge support by the U.S. Department of Energy, Office of Science, Basic Energy Sciences, Materials Science and Technology Division Grant No. DE-FG02-09ER46554 and by the McMinn Endowment at Vanderbilt University. Computations were performed at the National Energy Research Scientific Computer Center (a U.S. Department of Energy Office of Science User Facility located at Lawrence Berkeley National Laboratory, operated under contract no. DE-AC02-05CH11231. B.Z., M.S., and J.R. acknowledge support from an ARO MURI program (W911NF-21-1-0327), an ARO grant (W911NF-19-1-0137), and National Science Foundation (DMR-2122071). H.Z. and T.F. acknowledge support from National Science Foundation (NSF) (award number: CBET 2212830). H.Z. and T.F. used the computational resource of Bridges-2 at Pittsburgh Supercomputing Center through allocation PHY220002 from the Advanced Cyber infrastructure Coordination Ecosystem: Services & Support (ACCESS) program, which is supported by National Science Foundation grants #2138259, #2138286, #2138307, #2137603, and #2138296, National Energy Research Scientific Computing Center, a DOE Office of Science User Facility supported by the Office of Science of the U.S. Department of Energy under Contract No. DE-AC02-05CH11231 using NERSC award BES-ERCAP0022132, and Center for High Performance Computing (CHPC) at the University of Utah. G.B. thanks NSF award CMMI 2436601 that supported the work, in part. A.G. and S.T. acknowledge support from the Office of Naval Research Grant No. N00014-24-1-2419. This work was performed, in part, at the Center for Integrated Nanotechnologies, an Office of Science User Facility operated for the U.S. Department of Energy (DOE) Office of Science. Sandia National Laboratories is a multi-mission laboratory managed and operated by National Technology and Engineering Solutions of Sandia, LLC, a wholly owned subsidiary of Honeywell International, Inc., for the U.S. DOE's National Nuclear Security Administration under contract DE-NA-0003525. The views expressed in the article do not necessarily represent the views of the U.S. DOE or the United States Government.

Author contributions

M.S.B.H., E.R.H., and P.E.H. designed the experiments. B.Z., M.S., and J.R. synthesized the materials and performed XRD characterizations. D.B., H.Z., T.F., and S.T.P. performed the MLMD calculations. S.T. and A.G. performed the SED calculations. E.O. and G.B. performed the DFT calculations. K.H. and E.A.S. carried out the ion irradiation experiments. M.S.B.H., J.A.T., J.T.G., K.A., and S.M. carried out the thermal conductivity measurements. E.R.H. and J.A.H. performed the TEM and EELS characterizations. A.A. and A.M.H. performed the nanoindentation experiments. M.S.B.H., E.R.H., B.Z., D.B., A.G., J.R., S.T.P., and P.E.H. wrote the manuscript. All authors reviewed the manuscript.

Competing interests

The authors declare no competing interests.

Additional information

Supplementary information The online version contains supplementary material available at https://doi.org/10.1038/s41467-025-61078-5.

Correspondence and requests for materials should be addressed to Jayakanth Ravichandran, Sokrates T. Pantelides or Patrick E. Hopkins.

Peer review information *Nature Communications* thanks Aditya Sood, and the other, anonymous, reviewer(s) for their contribution to the peer review of this work. A peer review file is available

Reprints and permissions information is available at http://www.nature.com/reprints